The synergic impacts of salt mixture and frost damage on rock decay: implications for the deterioration of rock-hewn heritages

Yinghong Wang[1*] and Hui Zhang[1]

Abstract

Soluble salt and freeze–thaw are two significant weathering factors that contribute to the deterioration of rock-hewn heritages. Previous research has predominantly focused on the separate influences of salt weathering and freeze–thaw. However, in a realistic scenario, these two processes can occur simultaneously in nature, leading to a more complex decay process for such heritage. The aim of this study was to assess the combined impact of salt weathering and freeze–thaw on the severity of deterioration in rock-hewn heritage through evaluation of the variation of stone samples' appearance and physical–mechanical properties, such as deterioration patterns, pore structure, surface hardness and splitting tensile strength. A laboratory ageing test was conducted using materials and climatic conditions representative of the West Lake Cultural Landscape of Hangzhou (WLCL), a UNESCO World Heritage Site located in Southeast China. Five different types of stones were collected from the WLCL area and its vicinity and subjected to 25 ageing cycles, each consisting of three phases: salt impregnation, freezing-thaw, and evaporation. The mixture of $Na_2SO_4-MgSO_4$ was used as the contaminant substance. Results show that stones with moderate porosity (~ 5%) and a higher proportion of micropores, like flint, were susceptible to the combined effects of salt weathering and freeze–thaw, exhibiting significant surface deformation and strength decline. The porous tuff was primarily impacted by the development of a hard and thick crust on its surface, along with noticeable pore fill. The compact carbonate rock exhibited limited dimensional expansion with no discernible signs of deterioration patterns. Most rock specimens, except tuff, experienced a shift in their pore size distribution towards larger magnitudes, resulting in an increased average pore radius. This suggests that the inherent properties of rock-hewn heritages play a significant role in determining their vulnerability to various weathering agents. Consequently, these properties should serve as the foundation for developing future preventive conservation measures.

Keywords Rock-hewn heritages, Simulation ageing test, Salt mixture, Freeze–thaw, Pore structure

*Correspondence:
Yinghong Wang
yinghong.wang@zju.edu.cn
Full list of author information is available at the end of the article

Graphical Abstract

Introduction

The deterioration of stone heritages, including stone buildings, rock-hewn sites and stone carvings, is associated with rock breakdown led by the natural weathering processes. Salt weathering and freeze–thaw are recognised as the two leading causes of weathering and deterioration of rock heritage [1–4]. The common soluble salts in nature, such as sodium carbonate, sodium sulfate, sodium nitrate, sodium chloride, and magnesium sulfate, can lead to rock breakdown by repeatedly generating crystallisation pressure to the rock's pore wall when ambient temperature fluctuations [5–8]. Studies have shown that the degree of damage caused by salt weathering is affected by the solution supersaturation ratio and location of crystallisation, and these two influencing factors are directly controlled by the solution properties and evaporation rate [9]. Salt weathering often forms typical deterioration patterns on the rock surface, such as efflorescence, alveolization and exfoliation [10]. The most devastating deterioration pattern was discovered to be the subflorescence, i.e. salt crystals precipitated underneath the rock surface, and it was considered that the mass transport of soluble salt inside the rock and the rhythmic nature of crystallisation front is a dissipative structure [11]. These deterioration patterns are the macroscopic manifestation of changes in rock properties, especially rock's physical and mechanical properties [12, 13].

Freeze–thaw is another crucial cause of rock heritage deterioration [14]. When the ambient temperature reaches around 0 ℃, the water in rock pores, fissures and voids can crystallise into ice and expands in volume (9 vol.% under atmospheric conditions [15]. Previous studies have shown that the water inside the rock tends to flow from the small pores to the large pores, from the unfrozen area to the frozen area, and the capillary pressure and hydraulic pressure are formed during the flow process, which weakens the intergranular cohesion of rock grains [16, 17]. Like salt weathering, the freeze–thaw process also affects rocks' physical and mechanical properties [18]. For instance, the decrease in compressive strength and surface hardness occurs in sedimentary rock after freeze–thaw cycles [19], the volume increase of specifically oriented cracks induces the anisotropic response of elastic velocities [20], and changes in porosity, pore volume, pore size distribution after frozen damage [21].

Laboratory simulation is a typical means to study soluble salt weathering and freeze–thaw effects. Several standardised protocols have been proposed. For example, the European standards for the determination of frost resistance of natural stone [22] employ the simulation condition that is a 12-h cycle with temperature fluctuating between 20 ℃ and – 12 ℃, besides require to reach every set temperature within 0.5 h and inject water into the environmental chamber to fully immersing samples in every cycle. Although the BS EN standard shortens the simulation duration, the complexity of its operation increases the requirements for the degree of automation of the equipment, especially the environmental chamber.

The American Society for Testing and Materials [23] provides a freeze–thaw condition with a cycle of 24 h. The range of temperature during a freeze–thaw cycle is $- 18 \pm 2.5$ ℃ (16 h) to 32 ± 2.5 ℃ (8 h). This temperature range is more reflective of temperate to subtropical regions.

Similarly, some experimental standards have been published for laboratory simulations of salt damage. For instance, BS EN 12370 [24] proposes a salt resistance test method for natural rocks, which requires the rock samples to be completely immersed in sodium sulfate solution, then dried at 105 ℃, repeating the former steps until failure occurs on the samples. This test method can accelerate the ageing process. However, it is criticised for being less representative of the actual scenario because the drying temperature and the complete immersion with a salt solution are too extreme to be seen from stone structures in either natural or urban environments [25]. To ensure the reliability of the results, a new accelerated ageing test method has been proposed (RILEM TC 271-ASC [26]). It proposes to use sodium sulfate or sodium chloride as impregnating salts and simulate the salt weathering process by simultaneously controlling the temperature and humidity conditions during the ageing process. The simulation is conducive to investigating the salt damage induced by the deliquescence-recrystallisation process under changing humidity conditions. To examine the soluble salts present in stone heritage structures, such as rock buildings, the European standard UNE EN 16455:2016 [27] has been established. The extraction of solid samples is necessary for the analysis of soluble salts, and ion chromatography is recommended for the determination of chloride, nitrite, nitrate, sulfate, sodium, potassium, calcium, magnesium, and ammonium ions. Compared to the previous standardized method from NORMAL 13/83 [28], which involved stirring samples for 72 h, the latest standard specifies a shorter extraction time of 2 h. However, it is anticipated that the shorter extraction time may lead to lower extraction efficiency. To enhance the recovery of soluble salts, the use of ultrasound energy has been utilized [29–31].

The presence of soluble salts in nature and the variations in temperature and humidity across the four seasons result in the combined impact of salt weathering and freeze–thaw on rock's weathering and deterioration. As a result, the deterioration process of rocks is always more intricate compared to the standard simulation test that employs a single weathering factor [32–35]. The mixed saline solution, consisting of various anions and cations, is a common component of the hydrological system. This would lead to the precipitation of diverse salts from the solvent when temperature and humidity fluctuate. These include widely recognised single salts like mirabilite ($Na_2SO_4 \cdot 10H_2O$), thernadite (Na_2SO_4), epsomite ($MgSO_4$) and incongruently soluble double salts like bloedite ($Na_2Mg(SO_4)_2 \cdot 4H_2O$) and darapskite ($Na_3NO_3SO_4 \cdot H_2O$) [36, 37].

Rock-hewn heritages, such as cave temples, stone carvings, and rock-cut Buddha statues, hold significant cultural value in China. These artefacts provide valuable insight into Chinese history, religion, art, and the cultural exchanges between China and the West [38]. China possesses a vast collection of rock-hewn heritages. The National Cultural Heritage Administration of China conducted a comprehensive survey in 2020, revealing a total of 2155 cave temples and 3831 rock-cut statues in the country [39].

These remarkable cultural treasures face severe deterioration issues. For instance, Zhang et al. [40] observed pronounced granular disintegration, fragmentation, and salt deposition on the façade (120 m long and 30 m tall) of the notable North Grottoes Temple, a representative example in Northwest China. Additionally, Yu et al. [41] discovered extensive surface degradation, characterised by powdering, scaling, and efflorescence, in carbonate rock-hewn heritages in Southeast China. It was determined that 51% of these sites had reached a level of "serious" damage.

However, there remains a lack of research concerning the mechanisms underlying the deterioration of rock-hewn heritage, particularly the formation mechanisms of surface weathering driven by soluble salt and freeze–thaw. Hence, this study aims to evaluate the synergic impact of the salt mixture and frost damage on rock-hewn heritage and contribute to a comprehensive understanding of their weathering mechanism.

Methodology

An experimental workflow was developed to simulate the synergic effects of salt weathering and frost damage under realistic climatic conditions in a laboratory setting (see Fig. 1). The experiment involved the following steps: preparation of experimental materials, preparation of experimental materials, simulation ageing test, appearance observation and measurement of physic-mechanical properties.

To select the appropriate salts for the experiment, ion chromatography and the ECOS-RUNSALT thermodynamic model [42, 43] were used to identify the soluble salts in the historic stone building named Chuyangtai, located north of the World Heritage Site 'West Lake Cultural Landscape of Hangzhou'. Stone samples were collected from both the mountains within the West Lake Cultural Landscape and a nearby quarry in Hangzhou.

These samples were cut and grouped at the beginning of the experiment and then partially immersed
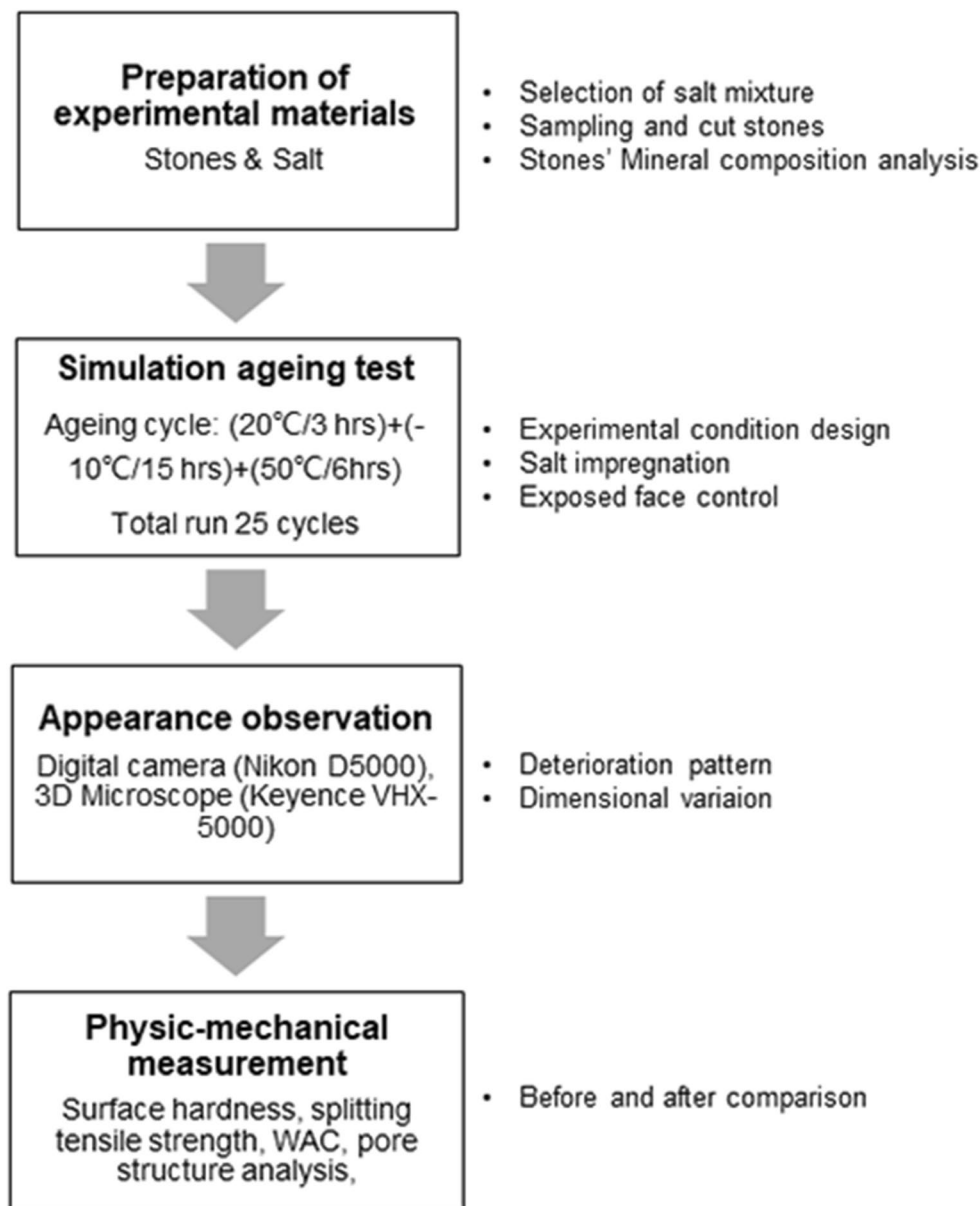
Fig. 1 Experimental workflow used in the salt weathering & freeze–thaw lab simulation. *WAC* water absorption coefficient through capillarity

in the saline solution until they reached a stable weight to impregnate them with salt. The stone specimens were then wrapped in polyethene foil, with one vertical face exposed, to mimic the vertical facade of the rock-hewn heritages. Subsequently, the samples underwent 25 cycles of the combined salt and freeze–thaw ageing test, followed by appearance observation and physical–mechanical properties determination. The original texture properties and mineral composition of rock were observed by a polarising microscope and determined by X-ray diffraction (Bruker SMART APEX II X-ray

diffractometer, operating at 40 kV and 40 mA with a Cu source, in the State Key Laboratory of Silicon Materials at Zhejiang University).

Selection of soluble salt

To identify the types of salts potentially present in the stone heritages of the West Lake, a salt assessment trial was conducted on the southeastern facade of the Chuyangtai. Three loose rock debris samples were collected from the facade (Fig. 2d) when the administration implemented a conservation project. The soluble salts in the

debris samples were extracted and analysed by the following steps:

a. The rock samples were ground into a fine powder.
b. A 1.0 g portion of the powdered rock sample was weighed and placed into a 50 ml plastic sample pot.
c. 50 ml of deionised water was added to the sample pot.
d. The liquid sample was sonicated for 1 h at room temperature and agitated for 1 h on a flask-shaker at 250 strokes per minute, followed by filtered into 100 ml volumetric flasks and made up to volume with deionised water.
f. Ion chromatography was used to determine the concentration of ions in the sample.
g. The ion content was inputted into the ECOS-RUNSALT model to predict the type of salts present.

For this study, a mixture of sodium sulfate and magnesium sulfate (1.4 mol/1.5 mol/kg) was chosen, as it represents the most common salt types found in our salt assessment trial on the southeastern facade of the Chuyangtai through ion chromatography and ECOS-RUNSALT prediction (Fig. 2a–c). Furthermore, it is known that the crystal phase precipitated from them can have destructive effects on stone-built heritages [44], such as bloedite ($Na_2Mg(SO_4)_2 \cdot 4H_2O$), which has been shown to have a high potential for damaging rock due to its characteristic of incongruent dissolution [37, 45].

Rock samples

The geological framework of the esteemed World Heritage Site 'Hangzhou West Lake Cultural Landscape' primarily consists of carbonate formations and volcanic formations [46]. Most of the rock-hewn heritages within this renowned site have been hewn from the cliffs of
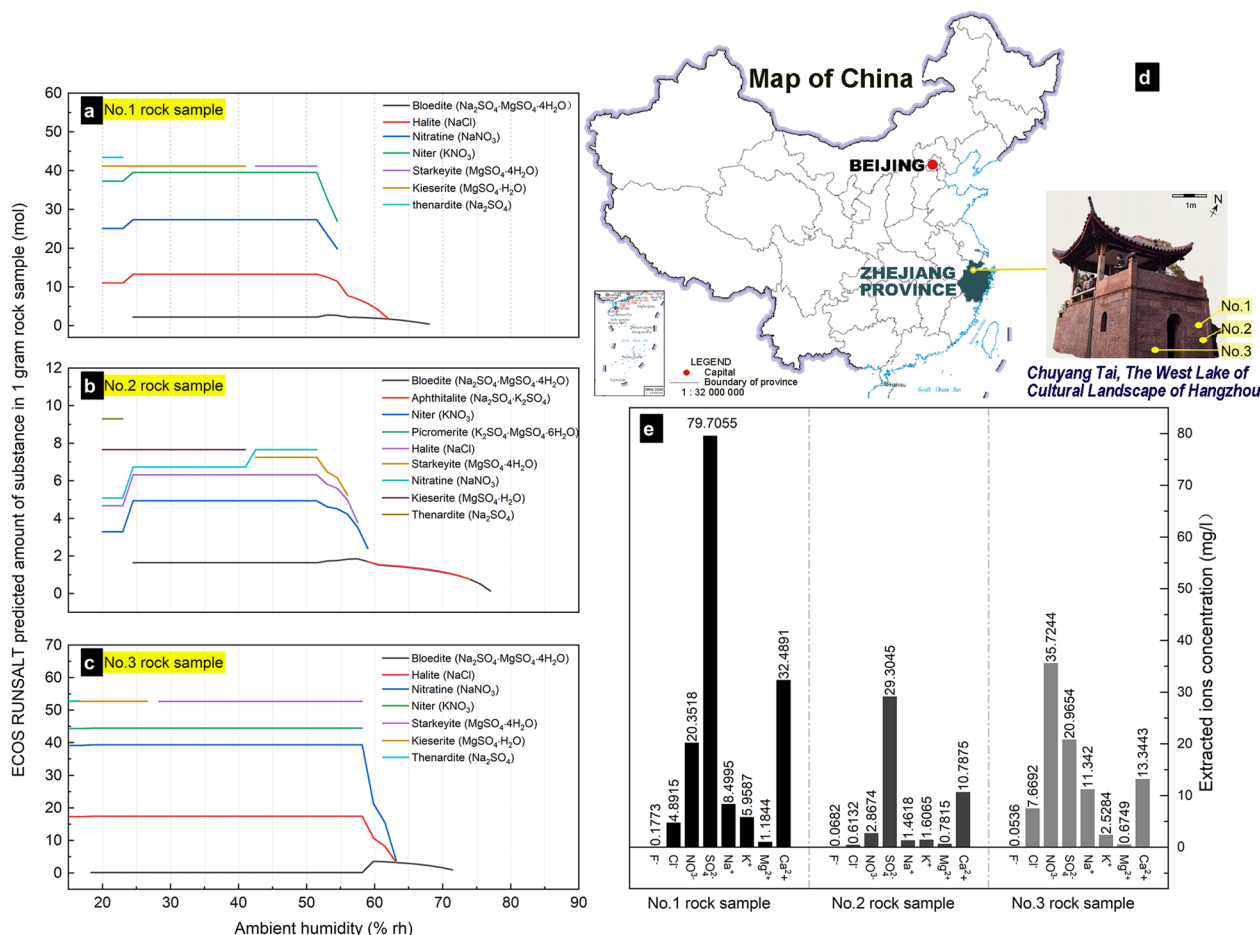

Fig. 2 Soluble salts extracted from the façade of the historic stone building (Chuyangtai) in Hangzhou, China. **a** ECOS-RUNSALT output diagram for the salts types predicted to be formed from the No.1 rock sample. **b** ECOS-RUNSALT output diagram for the salts types predicted to be formed from the No.2 rock sample. **c** ECOS-RUNSALT output diagram for the salts types predicted to be formed from the No.3 rock sample. **d** the image of Chuyangtai and its location. **e** ions concentration measured from the three rock samples through ion chromatography

limestone and volcanic rock [47]. Consequently, to study the synergic effects of the soluble salts and freeze–thaw cycles on the weathering of these significant artefacts, the study has chosen five typical indigenous rocks (Table 1). The petrographic characteristics and mineral composition information of the rock were obtained through polarizing microscope observation and X-ray diffraction analysis.

YM is a Permian limestone with a greyish white appearance and a coarse crystalline structure. Its main components are calcite $[CaCO_3]$ and calcium magnesium carbonate $[CaMg(CO_3)_2]$. This limestone was collected from the top of Yuhuang mountain, located in the southern part of the West Lake. The mountain is renowned for its ancient rock-hewn sites, including the Ciyunling rock-hewn statues, which were originally carved during the Wuyue Kingdom (907–978 CE).

LA is a Sinian flint with a pale-brown color and a cryptocrystalline structure. It consists mainly of quartz $[SiO_2]$, a small amount of muscovite $[KAl_2(AlSi_3O_{10})(OH)_2]$, and siderite $[FeCO_3]$. It was obtained from the Lin'an district, which is abun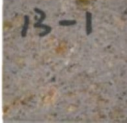dant in mineral resources such as limestone, kaolinite, tuff, and fluorite [48]. This district is situated approximately 35 km away from the West Lake.

FL is a carboniferous limestone with a grey color, displaying a microcrystalline matrix with sparite veins. Its primary constituents are calcite $[CaCO_3]$ and high Mg calcite $[CaMg(CO_3)_2]$. This limestone was sourced from the Feilai Feng peak, known for its ancient Buddha sculptures that were carved during the North Song dynasty (1282 CE). The peak is located to the northwest of the West Lake.

LQ is a freshly quarried Sinian dolostone from Banqiao, Lin'an district. It has a dark grey appearance and a microcrystalline structure. Its main components are Fe-dolomite $[Ca(Mg,Fe)(CO_3)_2]$ and dolomite $[CaMg(CO_3)_2]$. This essential carbonate rock is extensively used in the architecture industry.

GM is a Jurassic tuff with a pink color and a porphyritic texture of matrix. It consists mainly of quartz $[SiO_2]$, orthoclase $[K(AlSi_3O_8)]$, and muscovite $[KAl_2(AlSi_3O_{10})(OH)_2]$. It was sampled from Gu Mountain, an island within the West Lake. This mountain shares a similar

Table 1 Lithologic character, and basic Information about the stone samples

Sample name	Image of sample	stone type	Lithologic character	Age	Origin
YM		Limestone	Greyish white, coarse crystalline struture;mineral composition: Calcite[$CaCO_3$] and [$CaMg(CO_3)_2$]	Permian	Yuhuang mountain, Hangzhou, CN
LA		Flint	Pale-brown, cryptocrystalline structure; mineral composition: mainly quartz [SiO_2], a small amount of muscovite[$KAl_2(AlSi_3O_{10})(OH)_2$], and siderite [$FeCO_3$]	Sinian	Rulong county, Lin'an, Hangzhou, CN
FL		Limestone	Grey colored, microcrystalline calcite matrix with sparite veins; mineral composition: Calcite [$CaCO_3$] and high Mg calcite [$CaMg(CO_3)_2$]	Carboniferous	Feilai peak,Hangzhou, CN
LQ		Dolostone	Dark grey, microcrytalline,;mineral composition: Fe-dolomite [$Ca(Mg,Fe)(CO_3)_2$], and dolomite [$CaMg(CO_3)_2$]	Sinian	Quarry, Banqiao, Lin'an, CN
GM		Tuff	Pink, porphyritic tuff with cryptocrystalline texture of matrix; mineral composition: quartz [SiO_2], orthoclase [$K(AlSi_3O_8)$], muscovite $KAl_2(AlSi_3O_{10})(OH)_2$	Jurassic	Gu Mountain, Hangzhou, CN

diagenetic process and formation of rock minerals as Baoshi Mountain, which is home to several stone heritages [49].

Due to the limited availability of raw materials obtained from the field, YM was cut into four cuboids of dimensions 2.5 cm in length, 2 cm in width, and 5 cm in height. Similarly, LA was cut into three cuboids measuring 2.5 cm in length, 2 cm in width, and 3 cm in height. FL was cut into two cuboids with dimensions 4 cm in length, 3 cm in width, and 7.3 cm in height. As for LQ and GM, three cuboids of dimensions 3 cm in length, 1.2 cm in width, and 3 cm in height were produced, respectively.

Experimental conditions
The selected ageing conditions for the experiment (Fig. 3) were based on the documented extreme heat wave event that occurred during the summer of 2022 in Hangzhou, China [50], as well as the environmental parameters and time duration outlined in the standard freeze–thaw test methods ASTM D5312/D5312M-21 [23]. The ageing cycle consists of three distinct phases. In the first phase, known as the cooling and salt impregnation phase, the rock samples were partially immersed in a saline solution for three hours at room temperature (20 ℃). Following this, the frozen phase commenced, during which the samples were subjected to a temperature of − 10 ℃ for 15 h. Finally, the high-temperature phase, also known as the evaporation phase, involved subjecting the samples to a temperature of 50 ℃ for 6 h. Upon completion of the high-temperature phase, the next cycle was initiated from phase 1. The ageing testing procedure was carried out using the JINGHONG DHG-9000 oven and the AUCMA BC/BD-143DNE lab fridge, with a total of 25 cycles performed.
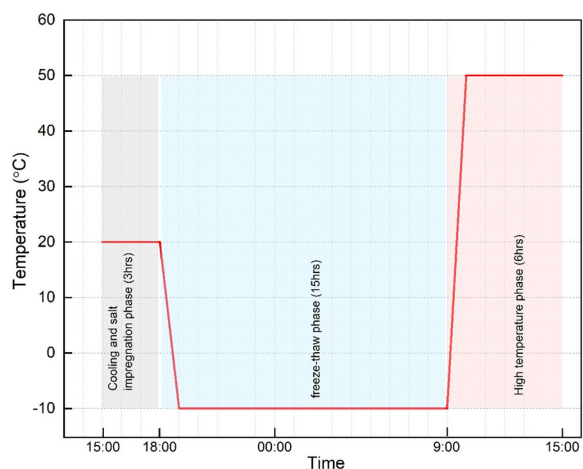

Fig. 3 Temperature cycle utilised for the rock ageing simulation

Dimensional change evaluation
The dimensional change coefficient (ε) of rock samples is determined by calculating the ratio of the change in length/width/height (Δx) of the sample after the ageing test to the original length/width/height of the sample (x_0), as represented in the following equations:

$$\varepsilon = \Delta x / x_o \cdot 100$$

$$\Delta x = x_i - x_o$$

where ε represents the dimensional change coefficient, x_0 denotes the sample's original length/width/height, and x_i refers to the sample's length/width/height after the ageing test.

Physic-mechanical properties measurement
Various measurements were conducted to assess the synergic impacts of salt weathering and frozen damage on the rock samples, including surface hardness, splitting tensile strength, water absorption coefficient by capillary (WAC), and pore structure analysis.

A Leeb hardness tester (BH200C, Guangzhou Botech Co., LTD) was used to measure the surface hardness. The BH200C is a high-precision Leeb hardness tester equipped with a D-type impact device. The impact device consists of a 3 mm diameter tungsten carbide ball with an impact energy of 11 mJ, which is consistent with the parameters of the widely recognized Equotip 550 (D-type impact head) Leeb hardness tester used in the field of rock heritage conservation [51]. Previous studies have demonstrated the reliability of this type of Leeb hardness tester for evaluating the extent of weathering on rock surfaces due to its portability, simplicity, low impact force (minimizing alterations to surface morphology), and sensitivity to the strength of the thin layer of weathered rock surface [52–54]. Therefore, we selected the BH200C Leeb hardness tester to assess the surface hardness of the rock samples in our study as a proxy for the degree of weathering. Following the sampling methods described by Aoki and Matsukura [55], ten rebound readings were obtained randomly hitting different points on the front vertical surface. The mean of these ten readings was then calculated.

The pore structures of YM, LA, FL, and GM were determined using the mercury intrusion porosimeter AutoPore IV 9510 (MIP) in the State Key Laboratory of Chemical Engineering at Zhejiang University. However, the porosity of LQ exceeded the minimum detection limit of the MIP, so the pore size distribution of LQ was instead analysed using the Quantachrome AUTOSORB-1-C gas sorption analyser [3]. The pore size distribution analysis utilised both density functional theory (DFT) and the Barrett-Joyner-Halenda method (BJH) [56].

However, it was found that the BJH method significantly underestimated the pore size for narrow mesopores with a diameter below approximately 10 nm. In contrast, DFT, which can describe the configuration of the adsorbed phase at the molecular level, was considered to provide a more reliable assessment of the pore size distribution across the entire nanoscale range [57–59]. The aforementioned finding that the BJH method underestimated the pore sizes of narrow mesopores is also present in this study's LA pore size distribution analysis. Therefore, the pore size distribution based on DFT was employed in this study.

The water absorption coefficient was measured according to the standard test protocol BS EN 1925:1999 [60]. The splitting tensile strength was determined following the ASTM standard C1006/C1006m-20a [61]. Due to the restriction towards rock sampling at the cultural heritage site, the availability of YM, LA, FL, and GM samples is limited, thus resulting in an insufficient number of samples that can only cater to the ageing group's requirements. Consequently, there is a lack of additional fresh samples that can be utilised for conducting the destructive splitting tensile strength test. In contrast, LQ samples were procured from non-heritage quarries, leading to a relatively abundant quantity of samples available for this destructive mechanical test. Thus, splitting tensile strength before and after the ageing test was obtained from LQ samples, while YM, LA, FL, and GM samples only obtained the properties after the ageing test.

Results and discussion
Appearance and dimensional changes
The vertical open surfaces in each group exhibit consistent changes and patterns of deterioration. Therefore, one specimen was selected from each group for presentation in Fig. 4. Figure 4 depicts the various effects of the ageing test on the appearance of the exposed vertical surfaces of the stone samples. In particular, the flint and tuff samples, referred to as LA and GM, respectively, demonstrate the most distinct variations.

In the case of the LA samples (Fig. 4b), blistering occurs on the stone surface after the ageing test, resulting in the delamination of the outer stone layer and a rise of 3801 µm. Fine salt efflorescence and point-like millimetric shallow cavities can also be observed on the raised elevations. These deteriorations significantly deform the LA surface.

For the GM samples (Fig. 4e), a thick, whisker-like crystal crust forms on the upper two-thirds of the open surface after the ageing test. This crust has a thickness of 2006 µm and is tightly bound to the surface, requiring a scalpel to be scraped off. Moreover, granular disintegration is also evident on the stone bottom.
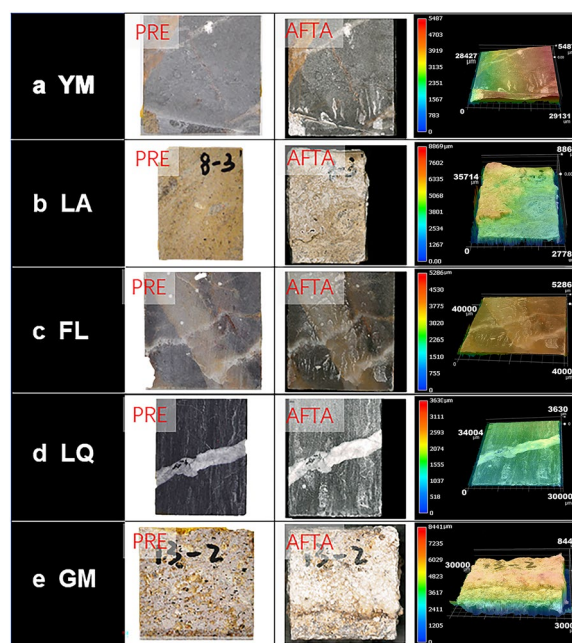

Fig. 4 Appearance changes of the five types of stone before and after the ageing test

On the contrary, the two limestone samples (YM and FL) and the dolostone sample (LQ) exhibit visually indistinguishable changes on their vertical exposed surfaces, with the exception of a small amount of salt efflorescence precipitating on the surface.

Under the simulated weathering conditions outlined in this study, the salt solution inside the rock underwent the following processes during the initial ageing cycle: capillary imbibition at room temperature, subzero freezing leading to the formation of ice crystals, dissolution of crystals at elevated temperatures, evaporation at high temperatures, and supersaturation resulting in recrystallisation [62]. Two thermodynamically stable phases, i.e. thenardite ($NaSO_4$) and bloedite ($Na_2Mg(SO_4)_2 \cdot 4H_2O$), were preferentially precipitated from [37, 63]. Bloedite generally appears as groups of plate-like crystals, forming spheroidal clusters [64]. On the other hand, thenardite has an elongated needle-like morphology, often grouped as dendrites [65]. These crystals play a role in adhesion during the first ageing cycle, glueing together rock grains and forming a thin crust on the evaporation front [11].

As the subsequent ageing cycle began, rock samples were impregnated with the salt solution. This re-impregnation of salt solution dissolves the thenardite and bloedite precipitated in the pores and increases the ion concentration, resulting in supersaturation within the pores and subsequent recrystallisation [66]. The dissolution of bloedite allows for the formation of additional crystals such as

hexahydrite ($MgSO_4 \cdot 6H_2O$), epsomite ($MgSO_4 \cdot 7H_2O$), bloedite ($Na_2Mg(SO_4)_2 \cdot 4H_2O$), and konyaite ($Na_2Mg(SO_4)_2 \cdot 5H_2O$) [37]. Although the aforementioned salt crystallisation may not co-occur, this will inevitably complicate the crystallisation process within the rock pores, leading to the generation of crystallisation pressures. Consequently, destruction may occur more significantly in the stage of the saline solution re-imbibition due to the transient high supersaturation ratio induced by the dissolution of salt crystals [67]. During the subsequent freeze–thaw stage, the ice chips would form inside the rock pore, further exerting pressure on the pore walls and exacerbating the ageing process. These repeated crystallisation-dissolution-supersaturation-recrystallisation processes damage the cohesion of rock grains, resulting in deterioration.

However, it is essential to emphasise that these weathering processes have distinct impacts on two different types of rocks, LA (flint) and GM (tuff). Based on the characteristics of destruction, it can be inferred that the deterioration patterns are related to the location of crystallisation, specifically the evaporation front. The surficial layer of LA rock delaminates from the body, which is considered to be caused by crystals formed underneath the surface. In contrast, no delamination or peeling was observed on the surface of GM rocks, but rather an abundance of salt crystals was deposited, signifying that crystallisation primarily occurs on the rock surface. The location of crystallisation, in turn, is influenced by porosity and pore size distribution, which will be further elucidated in Sect. "Pore structure characterisation".

According to the dimensional change coefficient (ε) results, different degrees of volume expansion were observed in all five groups of stone samples (Fig. 5). The GM samples (tuff) exhibited the highest dilation ratio (ε = 0.084% in width), which can be attributed to the precipitation of thick efflorescence on the rock surface. The LA sample (flint) exhibited the second-largest volume expansion rate, which is associated with surface delamination and deformation. It is worth noting that the three carbonate rocks, namely YM (limestone), FL (limestone), and LQ (dolostone), also showed relatively slight volume expansion, even though no visible signs of crust, erosion, or deformation were observed on their exposed vertical surfaces. This suggests the presence of residual strain in these carbonate rocks, potentially induced by the thermal expansion of calcite and dolomite during repeated heating [68]. Additionally, subflorescences may also be present beneath the lower part of the rock surface [69], but their influence is limited due to the low porosity, which is known to be correlated with low salt uptake [70].
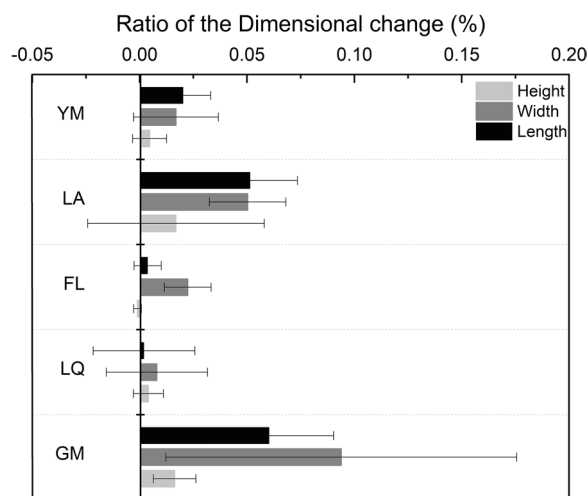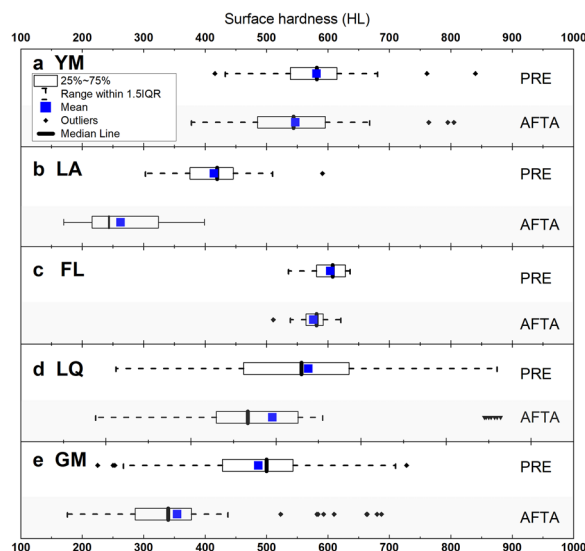

Fig. 5 Ratio of the dimensional change

Fig. 6 The boxplot of surface hardness before and after the ageing test. *PRE*-before the ageing test, *AFTA*-after the ageing test)

Mechanical properties

The surface hardness of each stone group is depicted in Fig. 6. As shown in the figure, all samples demonstrate a decrease in surface hardness following the simulated ageing test. The GM, LA, LQ, YM, and FL samples experience an average decrease of 45%, 37%, 35%, 6%, and 5% in surface hardness, respectively. In conjunction with Sect. "Appearance and dimensional changes", it is evident that the two types of rocks exhibiting the greatest decreases in surface hardness are the types with the most severe deterioration patterns and noticeable volume expansion, namely GM (tuff) and LA (flint). This suggests that the tuff and flint rocks examined in this study are

less resistant to salt damage and freeze–thaw combined weathering compared to carbonate rock.

Figure 7 illustrates the splitting tensile strength of rocks following an ageing test. Comparing the fresh LQ samples with the aged LQ samples, it is evident from the boxplot that the aged samples exhibit a narrower interquartile range (0.0069 kPa), a lower average splitting tensile strength (0.0049 kPa), and a shorter distance between the median and the maximum (0.0055 kPa). These findings indicate a significant decrease in the splitting tensile strength of LQ samples after undergoing the simulation ageing test. Furthermore, it is expected that the splitting tensile strength of the other more porous rocks used in this study should theoretically decrease after ageing. However, due to the lack of direct data, the exact extent of this decline cannot be determined, thus necessitating further research in future experiments.

Pore structure characterisation
Table 2 presents the porosity, average pore diameter (APD), water absorption coefficient by capillary (WAC), and specific surface area (SA$_{MBET}$) for the five rock types. The table reveals that LA, FL, and LQ experienced an increase in porosity, with LA samples showing a nearly 100% increase after the ageing test. Furthermore, the APD of LA, FL, and LQ also enlarged following the

simulated ageing test. In contrast, both YM and GM showed a decrease in porosity after ageing. It should be noted, however, that the porosity of YM samples was extremely low, possibly falling below the minimum detection limit of mercury intrusion porosimetry, hence overestimating the initial porosity derived from this method. Considering the similar lower porosity of the LQ sample obtained through the nitrogen adsorption method, it can be assumed that YM's initial porosity is likely lower than 0.35% obtained after ageing, and the APD are expected to increase rather than decrease. Based on this inference, it can be concluded that only the GM samples (tuff) present a significant decrease in porosity attributed to pore filling by salt crystals during ageing.

As depicted in Fig. 8, the specimens were compared before and after the ageing test to observe changes in the type of pore size distribution. For LA (Fig. 8c, d), the unequal bimodal pore size distribution transforms into a relatively equal unimodal pore size distribution, with a significant increase in the average pore size. In the case of LQ (Fig. 8g, h), the unequal bimodal pore size distribution shifts to an unequal trimodal pore size distribution, with a distinct new peak at 6.5 nm and an increase in the mean pore size. This suggests that pores with this diameter grow within the stone after undergoing the simulated ageing test. On the other hand, FL
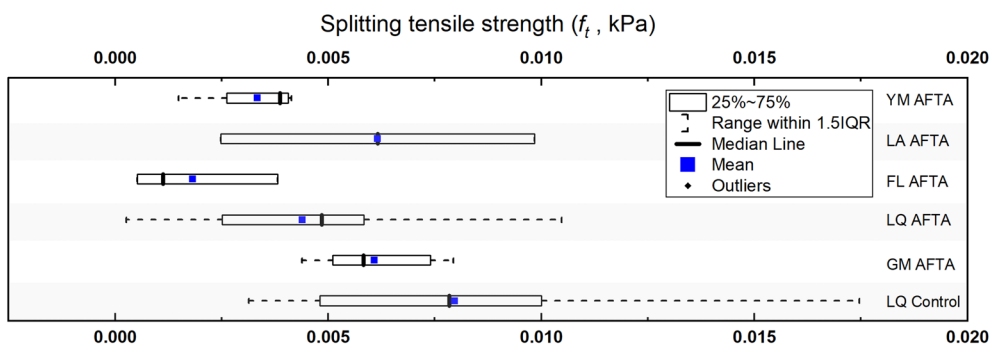

Fig. 7 Splitting tensile strength

Table 2 Pore structure analysis results and water absorption coefficient by capillary for the studied rocks

Sample name	Porosity (%)		APD (nm)		WAC (g m² s⁻⁰·⁵)		SA$_{MBET}$ (m²/g)*
	PRE	AFTA	PRE	AFTA	PRE	AFTA	AFTA
YM	1.54	0.35*	1095.925	38.05*	0.54829	0.77706	0.14
LA	5.93	11.50	19.8	97	3.36822	3.59301	16.03
FL	4.04	5.64	625.1	1778.7	0.3621	0.55393	0.12
LQ	0.32*	0.38*	18.79*	37.99*	1.04907	0.7139	0.40
GM	27.00	14.75	18.785	162.4	15.18607	8.40156	2.05

APD Average Pore Diameter, *PRE* before the salt and freeze–thaw test, *WAC* water absorption coefficient by capillary, *AFTA* after the salt and freeze–thaw test, *SA$_{MBET}$* multipoint BET surface area

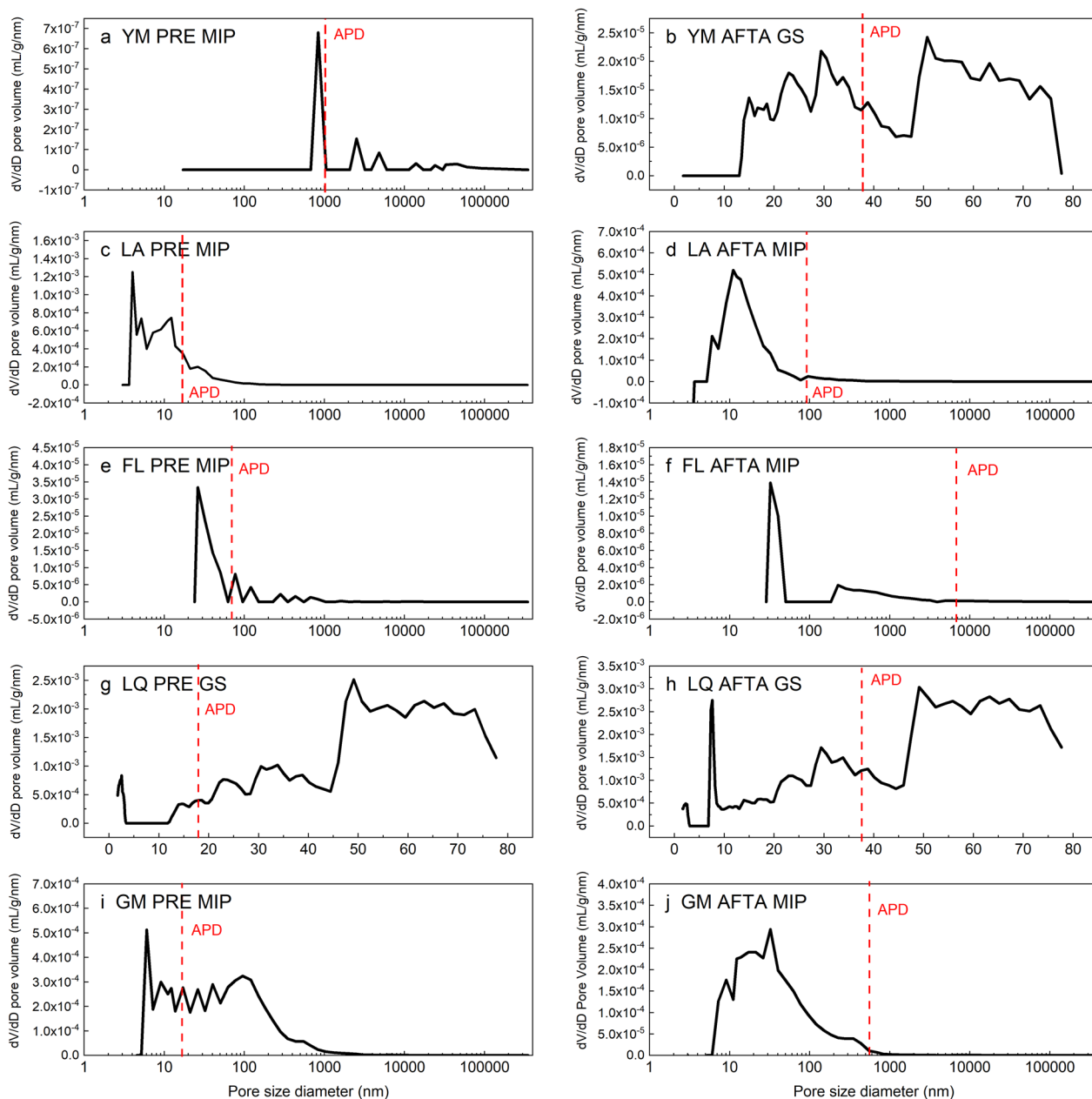*determined by Gas adsorption (nitrogen) method

Fig. 8 Schematic presentation of pore size distribution in the five types of rock (YM, LA, FL, LQ, GM) before (PRE) and after (AFTA) the simulation ageing test. *APD* average pore diameter, *MIP* determined through mercury intrusion porosimeter, *GS* determined through gas sorption analyser [nitrogen adsorption]

(Fig. 8e, f) maintains an unequal unimodal distribution after the ageing test, with a significant increase in the mean pore size. GM (Fig. 8i, j) undergoes a similar transformation in pore size distribution as LA, and the prominent peak shifts to a higher magnitude. Additionally, the proportion of larger pores (> 50 nm) and smaller pores (< 10 nm) in GM decreases, indicating that these pores, located near the upper and lower limits of the pore size distribution, tend to be preferentially filled during crystallisation.

Based on the analysis of two types of salt deposition patterns (subflorescence on LA flint and the efflorescence on GM tuff) in Sect. "Appearance and dimensional changes" and the pore structure of these two rocks, porosity and pore size distribution have been found to affect the deterioration patterns and destructive effects

significantly. According to Darcy's law, fluid flow speed is primarily determined by the porosity, permeability and density of porous media. In the same environment, a medium with lower porosity generally exhibits a lower flow rate than a medium with higher porosity [71, 72]. When the flow rate of the solution is lower than the evaporation rate, the front of evaporation will continue to recede, leading to the precipitation of crystals within the internal pores and the formation of more destructive subflorescence [9]. This could be a vital reason for the occurrence of subflorescence and surface deformation in LA rocks with lower porosity and relatively larger specific surface area. On the other hand, in GM rocks with higher porosity and larger average pore size, although this leads to increased salt absorption [70], a faster flow rate of the solution allows the salt solution to reach the rock surface more quickly, leading to deposition and the formation of efflorescence with less damage to the rock [73].

In addition, the size variations among the five different types of rock samples do have some impact on the total amount of soluble salt absorbed into the rock, i.e. salt uptake, although it is not a decisive factor. More precisely, as mentioned above, salt uptake is associated with the rock's porosity and pore size. For instance, under the same experimental conditions, rocks with a larger volume but low porosity and small pore diameter (such as YM and FL) may absorb less salt solution than rocks with a smaller volume but larger porosity and pore diameter (such as GM). Consequently, when there are fluctuations in ambient temperature and humidity, the larger-size rocks have fewer substances that can undergo the process of freezing, dissolving, crystallization, and recrystallization. As a result, the intensity of weathering is weakened. However, rocks with smaller sizes generally exhibit lower mechanical properties, such as surface hardness, than larger ones. Therefore, when evaluating the degree of rock weathering based on surface hardness, it is recommended to compare the rate of properties change before and after weathering rather than using direct data. All in all, numerous factors influence the resistance of rocks to weathering. For soluble salt and freeze–thaw combined weathering, the sample size affects the absorption of the salt solution by influencing the overall pore volume; besides, it also affects the initial mechanical strength. However, the type of deterioration patterns and ultimate extent of damage are more closely related to the porosity and pore size distribution.

Implication to the deterioration of rock-hewn heritage

The deterioration patterns and degree of weathering caused by the synergic impacts of salt mixture and freeze–thaw are determined by the intrinsic properties of the rock specimens. Among the five types of rock,

the porous flint (LA) and tuff GM) were found to be the most vulnerable. This suggests that heritages hewn from them are more susceptible to the combined effects of the salt weathering and freezing-thaw than those hewn from relatively compact carbonate stone. Therefore, it is necessary to be vigilant about the negative impact of salt and frost damage in the West Lake Cultural Landscape of Hangzhou,specifically those in the Baoshi and Gu Mountains that constitute of volcanic sedimentary rock, like tuff.

On the other hand, higher porosity leads to greater water absorption capacity, making the re-imbibition of saline solution the most harmful phase during the weathering process. This is due to the crystallization pressure generated by the dissolution and recrystallization of the deposited salt crystals inside the rock pores. This dangerous process is most likely to occur in rainy and humid climates. In comparison to the year-round climate conditions in Hangzhou, the summer with 'plum rain' (rainy season) and a hot and humid climate is the most unfavourable season for this type of rock-hewn heritage as these salts can reach their maximum destructive potential under such climatic conditions [74, 75].

The carbonate rocks (YM, FL, and LQ) show minimal visual changes but exhibit noticeable dimensional expansion, which is likely due to repeated heating during the high-temperature phase of the ageing cycle. This expansion poses a potential threat to the structural integrity of heritage sites hewn on these rocks. Given the humid subtropical climate of the West Lake Cultural Landscape of Hangzhou [76] and the escalating frequency of extreme high-temperature events in recent years [77], it is crucial to pay more attention to the damage caused by such thermal expansion on the carbonate rock-hewn heritages such as the renowned Feilai Feng Peak Buddha sculptures (1281–1292 CE) and Ciyunling Statues (942 CE) [78, 79].

Conclusion

The investigation of laboratory simulation of stone weathering, utilizing climate data from the heritage site and a standardized ageing test protocol, can yield more realistic outcomes of properties alteration, such as pore size distribution, water absorption, surface hardness, and changes in appearance, and unveil the deterioration mechanisms of the immovable cultural heritage, namely rock-hewn heritage. Consequently, it not only aids in comprehending the weathering process of local rock-hewn heritage but also facilitates comparisons with research on similar cultural heritage sites in different regions. This accumulation of reliable data and results contributes to a more comprehensive understanding of the drivers and mechanisms of weathering in rock-hewn heritage conservation.

The repeated salt contamination and freeze–thaw cycles caused different deterioration patterns on different stone types. Subflorescence was formed on the relatively porous flint (LA), leading to the destruction and deformation of its original appearance. A thick crust layer formed on the surface of the most porous sedimentary tuff (GM), covering the initial surface of the stone but less destruction on the stone's intactness. This emphasizes that rock-hewn heritages with moderate porosity (~ 5%) and a higher proportion of micropores are prone to experience more irreversibly destructive damage caused by subflorescence under a combined salt weathering and freeze-thawing effect.

In contrast, no evident visual changes happened on the three compact carbonate stones (YM, FL, and LQ), but volume expansion, which is more likely to be associated with repeated heat, also occurred. This is a potential threat to the temperature-sensitive carbonate rock-hewn heritage, especially those heritages in subtropical climates. Considering the continuously warming climate and increasing occurrence of extreme climatic events, like heat waves, heavy rain and flooding, there is an urgent need to cut off the direct contact between the rock and the atmospheric environment to mitigate further weathering and deterioration.

The aforementioned recognition indicates that rock heritage hewn from different rock types reacts differently to the same weathering driver. Porous materials like flint and tuff are more susceptible to the combined effects of soluble salts and freeze–thaw cycles compared to denser carbonate rocks. Consequently, when developing a preventive conservation strategy centred on environmental control, it is crucial to identify the primary weathering factors, the influential environmental parameters, and the conservation measures based on the specific rock type and its inherent properties, such as mineralogy composition and pore size distribution. Additionally, considering the immovable nature of rock-hewn heritage, it is essential to analyze the characteristic information pertaining to the surrounding environment connected to the site. With the comprehension of these factors, further efforts should be undertaken in the future to comprehensively assess the intrinsic properties of such rock-hewn heritage and the microenvironments surrounding them.
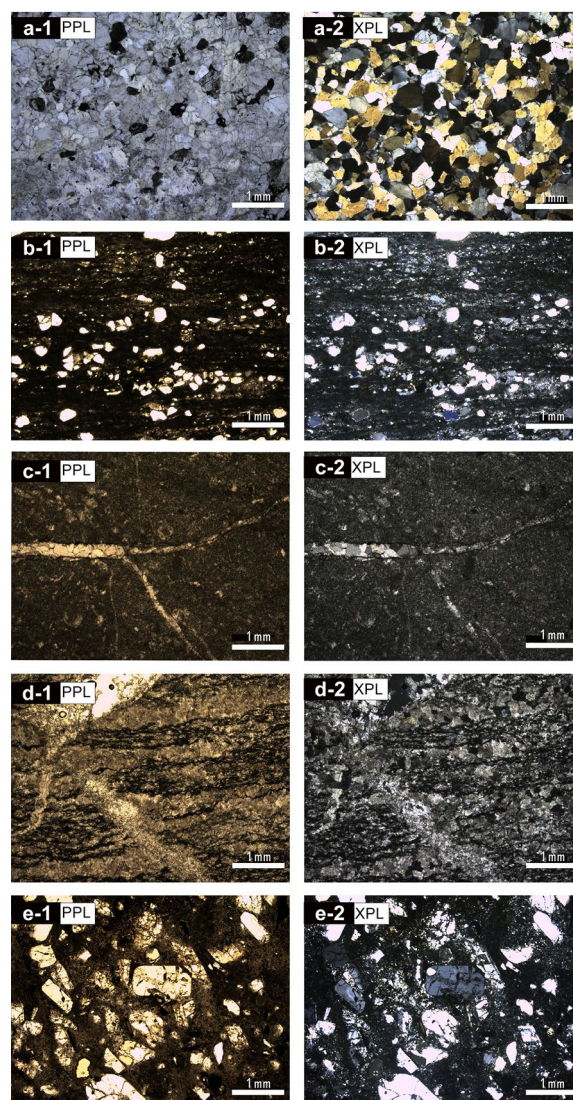
Appendix
See Fig. 9

Fig. 9 Microphotographs of the a-1 YM sample, b-1 LA sample, c-1 FL sample, d-1 LQ sample and e-1 sample under plane-polarized light (PPL); and a-2 YM sample, b-2 LA sample, c-2 FL sample, d-2 LQ sample and e-2 sample under cross-polarized light (XPL)

Declarations

Competing interests
The authors declare that they have no known competing financial interests or personal relationships that could have appeared to influence the work reported in this paper.

Author details
[1]School of Art and Archaeology, Zhejiang University, 148 Tianmushan Rd, Hangzhou 310028, Zhejiang, China.

References
1. Goudie AS, Viles H. Salt weathering hazards. Chichester: Willey; 1997.
2. Steiger M, Charola AE. Weathering and deterioration. In: Siegesmund S, Snethlage R, editors. Stone in architecture: properties, durability. Berlin: Springer Science & Business Media; 2011.
3. Siegesmund S, Durrast H. Physical and mechanical properties of rocks. In: Siegesmund S, Snethlage R, editors. Stone in architecture. Heidelberg Dordrecht London New York: Springer; 2011. p. P97-226.
4. Romero Bastidas M, Aguirre Ullauri MDC, Ramírez Bustamante J, Vargas Vallejo M, Castillo Carchipulla E. The quantification of physico-mechanical properties and durability of onyx-travertines from Santa Ana de los Ríos de Cuenca Ecuador. Herit Sci. 2022;10(1):194. https://doi.org/10.1186/s40494-022-00826-y.
5. Cooke RU, Smalley IJ. Salt weathering in deserts. Nature. 1968;220(5173):1226–7. https://doi.org/10.1038/2201226a0.
6. Goudie AS. Laboratory simulation of the wick effect in salt weathering of rock. Earth Surf Proc Land. 1986;11(3):275–85. https://doi.org/10.1002/esp.3290110305.
7. Robinson DA, Williams RB. Experimental weathering of sandstone by combinations of salts. Earth Surf Proc Landf. 2000;25(12):1309–15. https://doi.org/10.1002/1096-9837(200011)25:12%3c1309::AID-ESP139%3e3.0.CO;2-5.
8. Scherer GW. Stress from crystallisation of salt. Cem Concr Res. 2004;34(9):1613–24. https://doi.org/10.1016/j.cemconres.2003.12.034.
9. Rodriguez-Navarro C, Doehne E. Salt weathering: influence of evaporation rate, supersaturation and crystallisation pattern. Earth Surf Proc Land. 1999;24(3):191–209. https://doi.org/10.1002/(SICI)1096-9837(199903)24:3%3c191::AID-ESP942%3e3.0.CO;2-G.
10. Vergès-Belmin V. Illustrated glossary on stone deterioration patterns monuments and sites XV. Paris: ICOMOS; 2008.
11. López-Acevedo V, Viedma C, Gonzalez V, Viedma C. Salt crystallisation in porous construction materials. II. mass transport and crystallisation processes. J Cryst Growth. 1997;182(1–2):103–10. https://doi.org/10.1016/S0022-0248(97)00341-2.
12. La Iglesia A, González V, López-Acevedo V, Viedma C. Salt crystallisation in porous construction materials I estimation of crystallisation pressure. J Cryst Growth. 1997;177(1–2):111–8. https://doi.org/10.1016/S0022-0248(96)01072-X.
13. Benavente D, Cueto N, Martínez-Martínez J, García del Cura MA, Cañaveras JC. The influence of petrophysical properties on the salt weathering of porous building rocks. Environ Geol. 2007;52(2):215–24. https://doi.org/10.1007/s00254-006-0475-y.
14. Deprez M, De Kock T, De Schutter G, Cnudde V. A review on freeze-thaw action and weathering of rocks. Earth-Sci Rev. 2020;203:103143. https://doi.org/10.1016/j.earscirev.2020.103143.
15. Hirschwald J. Die Prüfung der natürlichen bausteine auf ihre wetterfeständigkeit. Berlin: W Ernst & Sohn; 1908.
16. Everett DH. The thermodynamics of frost damage to porous solids. Trans Faraday Soc. 1961;57:1541–51.
17. Eslami J, Walbert C, Beaucour AL, Bourges A, Noumowe A. Influence of physical and mechanical properties on the durability of limestone subjected to freeze-thaw cycles. Constr Build Mater. 2018;162:420–9. https://doi.org/10.1016/j.conbuildmat.2017.12.031.
18. Ruedrich J, Kirchner D, Siegesmund S. Physical weathering of building stones induced by freeze–thaw action: a laboratory long-term study. Environ Earth Sci. 2011;63:1573–86. https://doi.org/10.1007/s12665-010-0826-6.
19. Sarici DE, Ozdemir E. Determining point load strength loss from porosity, schmidt hardness, and weight of some sedimentary rocks under freeze–thaw conditions. Environ Earth Sci. 2018;77:1–9. https://doi.org/10.1007/s12665-018-7241-9.
20. Ivankina TI, Zel IY, Petruzalek M, Rodkin MV, Matveev MA, Lokajicek T. Elastic anisotropy, permeability, and freeze-thaw cycling of rapakivi granite. Int J Rock Mech Min Sci. 2020;136:104541. https://doi.org/10.1016/j.ijrmms.2020.104541.
21. Deprez M, De Kock T, De Schutter G, Cnudde V. The role of ink-bottle pores in freeze-thaw damage of oolithic limestone. Constr Build Mater. 2020;246:118515. https://doi.org/10.1016/j.conbuildmat.2020.118515.
22. BS En [British Standard Institution]. Natural stone test methods-determination of frost resistance (12371: 2010). London: BSI Standards; 2010.
23. ASTM [American Society for Testing and Materials]. Standard test method for evaluation of durability of rock for erosion control under freezing and thawing conditions (D5312/D5312M-21). 2021. https://www.astm.org/d5312_d5312m-21.html. Accessed 25 Sep 2023.
24. BS En [British Standard Institution]. Natural stone test methods. determination of resistance to salt crystallisation (12370:2020). London: BSI Standards; 2020.
25. Flatt RJ, Aly Mohamed N, Caruso F, Derluyn H, Desarnaud J, Lubelli B, Espinosa-Marzal RM, Pel L, Rodriguez-Navarro C, Scherer GW, Shahidzadeh N, Steiger M. Predicting salt damage in practice: a theoretical insight into laboratory tests. RILEM Tech Lett. 2017;2:108–18. https://doi.org/10.21809/rilemtechlett.2017.41.
26. Lubelli B, Rörig-Daalgard I, Aguilar AM, Aškrabić M, Beck K, Bläuer C, Cnudde V, D'Altri AM, Derluyn H, Desarnaud J, Diaz Gonçalves T. Recommendation of RILEM TC 271-ASC: New accelerated test procedure for the assessment of resistance of natural stone and fired-clay brick units against salt crystallisation. Mater Struct. 2023;56(5):101. https://doi.org/10.1617/s11527-023-02158-0.
27. UNE EN [Spanish Association for Standardization] Conservation of cultural heritage—extraction and determination of soluble salts in natural stone and related materials used in and from cultural heritage (16455:2016). 2016.
28. Normal 13/83 recommendation: determination of total amount of soluble salts. consiglio nazionale delle ricerche and istituto centrale del restauro (CNR-ICR) (1983).
29. Iñigo AC, Alonso R, Vicente-Tavera S. Dissolution of salts crystallised in building materials using ultrasound: an alternative to NORMAL (1983) standard methodology. Ultrason Sonochem. 2001;8(2):127–30. https://doi.org/10.1016/S1350-4177(00)00062-6.
30. Prieto-Taboada N, Gómez-Laserna O, Martinez-Arkarazo I, Olazabal MA, Madariaga JM. Optimization of two methods based on ultrasound energy as alternative to European standards for soluble salts extraction from building materials. Ultrason Sonochem. 2012;19(6):1260–5. https://doi.org/10.1016/j.ultsonch.2012.03.002.
31. Vázquez-de la Fuente I, Prieto-Taboada N, Lama E, Cristobal D, García-Arrona R, Arana G, Madariaga JM. The relevance of the use of ionic chromatography for the quantification of soluble salts in the analysis of built heritage: improving the European norms. Microchem J. 2023. https://doi.org/10.1016/j.microc.2023.108921.
32. Cardenes V, Mateos FJ, Fernández-Lorenzo S. Analysis of the correlations between freeze–thaw and salt crystallisation tests. Environ Earth Sci. 2014;71:1123–34. https://doi.org/10.1007/s12665-013-2516-7.
33. Jamshidi A, Nikudel MR, Khamehchiyan M. Evaluation of the durability of Gerdoee travertine after freeze–thaw cycles in fresh water and sodium sulfate solution by decay function models. Eng Geol. 2016;202:36–43. https://doi.org/10.1016/j.enggeo.2016.01.004.
34. Heidari M, Torabi-Kaveh M, Mohseni H. Assessment of the effects of freeze–thaw and salt crystallisation ageing tests on anahita temple stone, Kangavar, West of Iran. Geotech Geol Eng. 2017;35:121–36. https://doi.org/10.1007/s10706-016-0090-y.

35. Celik MY, Korucu MR. The effect of freeze-thaw cycles performed with salt solutions (NaCl and Na2SO4) on carbonate building stones. Bull Eng Geol Env. 2023;82(3):64. https://doi.org/10.1007/s10064-023-03072-z.

36. Lindström N, Heitmann N, Linnow K, Steiger M. Crystallisation behavior of $NaNO_3$–Na_2SO_4 salt mixtures in sandstone and comparison to single salt behavior. Appl Geochem. 2015;63:116–32. https://doi.org/10.1016/j.apgeochem.2015.07.007.

37. Lindström N, Talreja T, Linnow K, Stahlbuhk A, Steiger M. Crystallisation behavior of Na_2SO_4–$MgSO_4$ salt mixtures in sandstone and comparison to single salt behavior. Appl Geochem. 2016;2016(69):50–70. https://doi.org/10.1016/j.apgeochem.2016.04.005.

38. Su B. The review of the archaeology in cave temples. Cult Relics. 1979;10:7–9.

39. Li R. Announcing the latest cave temple survey results—the national cultural heritage held the "14th five-year" Cave temples conservation and archaeological work conference. 2021. https://translate.google.co.uk/?sl=en&tl=zh-CN&text=hosted%20%0Aheld&op=translate Accessed 8 May 2023.

40. Zhang JK, Zhang LX, Guo QL, Li WH, Wen X, Liu D. Research on the relationship between surface weathering characteristics and formation lithology of North Grottoes temple in Qingyang. J Northwest Univ (Natl Sci Edit). 2021;51(03):344–52. https://doi.org/10.16152/j.cnki.xdxbzr.2021-03-002.

41. Yu J, Zhang B, Shao P, Feng B. A survey on the state assessment of cave temples and rock carvings in Zhejiang Province. Stone. 2018;325(03):29–36.

42. Bionda, D. RUNSALT—A graphical user interface to the ECOS thermodynamic model for the prediction of the behaviour of salt mixtures under changing climate conditions. 2005. http://science.sdf-eu.org/runsalt/. Accessed 19 Feb 2022

43. Price CA. An expert chemical model for determining the environmental conditions needed to prevent salt damage in porous materials European commission research report No 11 protection and conservation of European cultural heritage. London: Archetype Publications; 2000.

44. Oguchi CT, Yu S. A review of theoretical salt weathering studies for stone heritage. Prog Earth Planet Sci. 2021;8(1):1–23. https://doi.org/10.1186/s40645-021-00414-x.

45. Wang Y, Viles H, Desarnaud J, Yang S, Guo Q. Laboratory simulation of salt weathering under moderate ageing conditions: implications for the deterioration of sandstone heritage in temperate climates. Earth Surf Proc Land. 2021;46(5):1055–66. https://doi.org/10.1002/esp.5086.

46. Xu YS, Shen JS, Zhou AN, Arulrajah A. Geological and hydrogeological environment with geohazards during underground construction in Hangzhou: a review. Arab J Geosci. 2018;11:1–18. https://doi.org/10.1007/s12517-018-3894-7.

47. UNESCO WHC [UNESCO World Heritage Convention]. West lake cultural landscape of Hangzhou. 2011. https://whc.unesco.org/en/list/1334/maps/ Accessed 19 May 2023.

48. LPNB [Lin'an Planning and Nat Resources Bureau]. List of mines with valid mining licenses in Lin'an District. 2019. http://www.linan.gov.cn/art/2019/8/1/art_1229293352_2747465.html. Accessed 29 Mar 2023.

49. Fu YH. On the geological landscapes heritages and their significances of West Lake and its surrounding area in Hangzhou. Georeview. 2020;66(02):475–84. https://doi.org/10.16509/j.georeview.2020.02.016.

50. Mallapaty S. China's extreme weather challenges scientists studying it. Nature. 2022;609(7929):888. https://doi.org/10.1038/d41586-022-02954-8.

51. Wilhelm K, Viles H, Burke Ó. Low impact surface hardness testing (Equotip) on porous surfaces–advances in methodology with implications for rock weathering and stone deterioration research. Earth Surf Proc Land. 2016;41(8):1027–38. https://doi.org/10.1002/esp.3882.

52. Viles H, Goudie A, Grab S, Lalley J. The use of the schmidt hammer and equotip for rock hardness assessment in geomorphology and heritage science: a comparative analysis. Earth Surf Proc Land. 2011;36(3):320–33. https://doi.org/10.1002/esp.2040.

53. Wilhelm K, Viles H, Burke O, Mayaud J. Surface hardness as a proxy for weathering behaviour of limestone heritage: a case study on dated headstones on the Isle of Portland UK. Environ Earth Sci. 2016;75:931. https://doi.org/10.1007/s12665-016-5661-y.

54. Garrido ME, Petnga FB, Martínez-Ibáñez V, Serón JB, Hidalgo-Signes C, Tomás R. Predicting the uniaxial compressive strength of a limestone exposed to high temperatures by point load and Leeb rebound hardness testing. Rock Mech Rock Eng. 2022;55(1):1–17. https://doi.org/10.1007/s00603-021-02647-0.

55. Aoki H, Matsukura Y. A new technique for non-destructive field measurement of rock-surface strength: an application of the equotip hardness tester to weathering studies. Earth Surf Proc Land. 2007;32(12):1759–69. https://doi.org/10.1002/esp.1492.

56. Thommes M, Kaneko K, Neimark AV, Olivier JP, Rodriguez-Reinoso F, Rouquerol J, Sing KS. Physisorption of gases, with special reference to the evaluation of surface area and pore size distribution (IUPAC technical report). Pure Appl Chem. 2015;87(9–10):1051–69. https://doi.org/10.1515/pac-2014-1117.

57. Lowell S, Shields JE, Thomas MA, Thommes M. Characterisation of porous solids and powders: surface area, pore size and density, vol. 16. Berlin: Springer Science & Business Media; 2006.

58. Landers J, Gor GY, Neimark AV. Density functional theory methods for characterisation of porous materials. Colloids Surf, A. 2013;437:3–32. https://doi.org/10.1016/j.colsurfa.2013.01.007.

59. Thommes M, Cychosz KA. Physical adsorption characterisation of nanoporous materials: progress and challenges. Adsorption. 2014;20(2–3):233–50. https://doi.org/10.1007/s10450-014-9606-z.

60. BS En [British Standard Institution]. Natural stone test methods-determination of water absorption coefficient by capillarity (1925:1999). London: BSI Standards; 1999.

61. ASTM [American Society for Testing and Materials]. Standard test method for splitting tensile strength of masonry units (C1006/C1006M—20a). 2020. https://compass.astm.org/document/?contentCode=ASTM%7CC1006_C1006M-20A%7Cen-US

62. Winkler E. Stone in architecture: properties, durability. Berlin Heidelberg New York: Springer-Verlag; 1997.

63. Gumuzzio J, Batlle J, Casas J. Mineralogical composition of salt efflorescences in a typic salorthid. Spain Geoderma. 1982;28(1):39–51. https://doi.org/10.1016/0016-7061(82)90039-8.

64. Buck BJ, Wolff K, Merkler DJ, McMillan NJ. Salt mineralogy of Las Vegas Wash, Nevada: morphology and subsurface evaporation. Soil Sci Soc Am J. 2006;70(5):1639–51. https://doi.org/10.2136/sssaj2005.0276.

65. Rodriguez-Navarro C, Doehne E, Sebastian E. How does sodium sulfate crystallise? Implications for the decay and testing of building materials. Cem Concr Res. 2000;30(10):1527–34. https://doi.org/10.1016/S0008-8846(00)00381-1.

66. Flatt RJ. Salt damage in porous materials: how high supersaturations are generated. J Cryst Growth. 2002;242(3–4):435–54. https://doi.org/10.1016/S0022-0248(02)01429-X.

67. McMahon D J, Sandberg P, Folliard K, Mehta P K. Deterioration mechanisms of sodium sulfate. In Proceedings of the 7th international congress on deterioration and conservation of Stone: held in Lisbon, Portugal, 1992. pp. 705–714.

68. Siegesmund S, Ullemeyer K, Weiss T, Tschegg EK. Physical weathering of marbles caused by anisotropic thermal expansion. Int J Earth Sci. 2000;89:170–82. https://doi.org/10.1007/s005310050324.

69. Gómez-Laserna O, Olazabal MÁ, Morillas H, Prieto-Taboada N, Martinez-Arkarazo I, Arana G, Madariaga JM. In-situ spectroscopic assessment of the conservation state of building materials from a Palace house affected by infiltration water. J Raman Spectrosc. 2013;44(9):1277–84. https://doi.org/10.1002/jrs.4359.

70. Yu S, Oguchi CT. Role of pore size distribution in salt uptake, damage, and predicting salt susceptibility of eight types of Japanese building stones. Eng Geol. 2010;115(3–4):226–36. https://doi.org/10.1016/j.enggeo.2009.05.007.

71. Whitaker S. Flow in porous media I: a theoretical derivation of Darcy's law. Transp Porous Med. 1986;1:3–25. https://doi.org/10.1007/BF01036523.

72. Xue L, Guo X, Chen H. Fluid Flow in Porous Media: fundamentals and applications. Singapore: World Scientific Publishing; 2021.

73. Norouzi Rad M, Shokri N. Nonlinear effects of salt concentrations on evaporation from porous media. Geophys Res Lett. 2012. https://doi.org/10.1029/2011GL050763.

74. Goudie AS, Viles H. 12 Weathering hazards. In: Alcantara I, Goudie AS, editors. Geomorphological hazards and disaster prevention. Cambridge: Cambridge University Press; 2010. p. 145.

75. Brimblecombe P, Grossi CM, Harris I. Climate change critical to cultural heritage. In: Gökçekus H, Türker U, LaMoreaux JW, editors. Survival and sustainability: environmental concerns in the 21st century. Berlin,

Heidelberg: Springer; 2011. p. 195–205. https://doi.org/10.1007/978-3-540-95991-5.

76. Zheng D. Study on the ecogeographical regional system in China. Beijing: The Commercial Press; 2008. p. 366.
77. WMO [World Meteorological Organization]. Provisional state of the global climate 2022. 2023. https://library.wmo.int/index.php?lvl=notice_display&id=22156#.ZCzbhXbP1dh. Accessed 5 Apr 2023
78. Chang Q. Zixian temple, ciyunling statues Hangzhou. Cult Relics. 1995;10(70–79):98.
79. Dong Y. Discussion on the Arhat Group in Yuru Cave, Feilai Feng Peak, Hangzhou. In: Hangzhou Normal University Art Education Research Institute, editor. Study on the art of west lake grottoes. Hangzhou: Xileng Book Press; 2019. p. 132–51.

Publisher's Note

Springer Nature remains neutral with regard to jurisdictional claims in published maps and institutional affiliations.